PERGAMON

International Journal of Heat and Mass Transfer 42 (1999) 3967–3981

International Journal of HEAT and MASS TRANSFER

www.elsevier.com/locate/ijhmt

Development and validation of an advanced turbulence model for buoyancy driven flows in enclosures

F. Liu [1], J.X. Wen*

School of Mechanical, Aeronautical and Production Engineering, Kingston University, Roehampton Vale, Friars Avenue, London SW15 3DW, UK

Received 31 March 1998; received in revised form 8 February 1999

Abstract

A new buoyancy-modified turbulence model is developed on the basis of the four-equation model, k–ε–$\overline{\theta^2}$–ε_θ, of Hanjalic [K. Hanjalic, S. Kenjeres and F. Durst, Natural convection in partitioned two-dimensional enclosures at higher Rayleigh numbers, Int. J. Heat Mass Transfer 39(7) (1996) 1407–1427]. The strong anisotropy of Reynolds stresses due to buoyancy effects in the vertical boundary layers is considered by inclusion of the newly devised 'return-to-isotropy' concept in the pressure-strain correlation. The wall-reflection functions is also duly modified. The new model has been tested in buoyancy-driven cavity flows through comparison with published experimental data and the predictions from three other turbulence models [N. Z. Ince and B. E. Launder, On the computation of buoyancy-driven turbulent flows in rectangular enclosures, Int. J. Heat and Fluid Flow 10(2) (1998) 110–117; K. Hanjalic, S. Kenjeres and F. Durst, Natural convection in partitioned two-dimensional enclosures at higher Rayleigh numbers, Int. J. Heat Mass Transfer 39(7) (1996) 1407–1427]. It has demonstrated significant improvements in capturing the non-isotropy of Reynolds stresses and turbulent heat flux in vertical boundary layers.

1. Introduction

The cavity type of flow and heat transfer phenomena is encountered in many engineering practices, e.g. room heating, cooling of electrical and electronic equipment, crystal growth, flows in nuclear reactor and fire-induced smoke spread, etc. All these enclosure flows are commonly dominated by buoyancy and near wall effects. Being simple in geometry and boundary conditions, cavity flows represent a simplified version of these practical scenarios. As a result, this generic type of physical phenomena has served and is continuing to serve as numerical and experimental benchmark tests for the development and validation of turbulence modelling strategies which can then be applied, with confidence, to buoyancy-driven enclosure flows in industrial applications. For this reason, turbulent natural convection has attracted considerable attention from the CFD community.

For enclosure flows where the Rayleigh numbers, Ra, fall in the range of 10^8–10^{12}, there exist several distinct scale flow patterns, which are dominated by different turbulent mechanisms. This well organised coherent structure is widely regarded as hardly tractable by the single point Reynolds averaging method [9]. For the cases of heating and cooling from vertical sides, the turbulence is trapped in relatively narrow zones in the downstream portions of the boundary layers along the non-adiabatic vertical walls, while the

* Corresponding author.

[1] Present address: CHAM Ltd, Bakery House, 40 High Street, Wimbledon, London SW19 5AU, UK

0017-9310/99/$ - see front matter
PII: S0017-9310(99)00073-3

Nomenclature

C_1, C_2, C_3	coefficient in Eq. (16)
$C_{1\theta w}$	coefficient in Eq. (13)
C_{ij}	convective flux for stress tensor
C_k	convective flux for turbulent kinetic energy
$C_{\varepsilon 1}$, $C_{\varepsilon 2}$	coefficients in Eq. (6)
$C^{\theta}_{\varepsilon 1}$, $C^{\theta}_{\varepsilon 2}$, $C^{\theta}_{\varepsilon 3}$, $C^{\theta}_{\varepsilon 4}$	coefficients in Eq. (7)
C_ϕ	coefficient in Eq. (11)
c_1	coefficient in Eq. (13)
D_ε	diffusive flux for ε
$D_{\varepsilon\theta}$	diffusive flux for ε_θ
D_ϕ	diffusive flux in Eqs. (4)–(7)
D_θ	diffusive flux for temperature variance
D_{ij}	diffusive flux for stress tensor
D_k	diffusive flux for turbulent kinetic energy
E	molecular effects, Eq. (6)
E_θ	molecular effects, Eq. (7)
f_ε, $f_{\varepsilon\theta}$	damping functions in Eqs. (6) and (7)
f_s	damping function in Eq. (15)
f_μ	damping function of Jones and Launder
g	gravitational accelerator
g_i	gravitational vector
G	buoyancy production for k
G_{ij}	buoyancy production for $\overline{u_j u_j}$
H	height of tall cavity
k	turbulent kinetic energy
L	width of square cavity
n_i, n_j, n_k	unit vector normal to walls
p	mean pressure
P	shear production for k
P_θ	production for temperature variance
P_{ij}	shear production for $\overline{u_j u_j}$
Ra	Rayleigh number
Re_t	turbulent Reynolds number
t	time
T	mean temperature
U	horizontal component of mean velocity
u_i	velocity fluctuation in i direction
U_i	mean velocity component in i direction
$\overline{u_i u_j}$	turbulent stress tensor
$\overline{u_i\theta}$, $\overline{u_j\theta}$	turbulent heat flux vector
$\overline{v\theta}$	vertical component of turbulent heat flux
V	vertical component of mean velocity
v	vertical component of velocity fluctuation
x_i	co-ordinate along i direction
x_n	distance normal to walls

Greek symbols

α, α_t	molecular and turbulent diffusivities
α_{ij}	anisotropy of Reynolds stresses
β	thermal expansion factor
δ_{ij}	$=1$, if $i=j$; $=0$, if $i\neq j$ in Eq. (21)
ε	dissipation rate of turbulent kinetic energy
ε_θ	dissipation rate of temperature variance
$\tilde{\varepsilon}$, $\tilde{\varepsilon}_\theta$	homogenous parts of ε and ε_θ
ε_θ	dissipation rate tensor for temperature variance
ε_{ij}	dissipation rate tensor for $\overline{u_i u_j}$
ξ	empirical coefficient, Eq. (12)
η	empirical coefficient, Eq. (12)
φ_{ij}	pressure correlation for $\overline{u_i u_j}$
φ_{ij1}	turbulence–turbulence part of φ_{ij}
φ_{ij2}	mean-strain part of φ_{ij}
φ_{ij3}	buoyancy force part of φ_{ij}
φ_{ijw}	wall-reflection part of φ_{ij}
$\varphi_{i\theta w}$	wall-reflection part of pressure-scaler correlation
μ	molecular viscosity
ρ	density
σ_t	turbulent Prandtl number of T
$\overline{\theta^2}$	temperature variance

core region remains largely stratified and laminar. Besides the large scale rotation in the enclosure, evidence from numerical calculations and experiments shows some secondary flows around the corners, hard to detect at lower Ra numbers and conspicuous at higher Ra numbers [1]. The velocity and temperature gradients in the boundary layers are strongly affected by the buoyancy force, the presence of the solid wall and molecular viscosity. The buoyancy effects are immediately felt by the flow in the so-called buoyant sub-layer, the upper part of the inner sub-layer within the boundary layer [10].

In order to introduce the present model, it is felt necessary to briefly review some relevant aspects in the development of turbulence models for buoyancy-driven flows while more detailed reviews can be found in Refs. [11,23].

1.1. Near wall effects

To account for the near wall effects, previous researchers have adopted two methods: wall functions and low-Re-number modifications. The first group, represented by George and Capp [12] and

Cheesewright [13], used the modified wall functions concept, originally derived for high Reynolds number forced convection flows, to avoid the need for fine grid mesh to be allocated in the sub-layer for cheap computational costs. But the strong dependence on particular characteristic parameters to certain flow patterns and the lack of generality have very much limited the applications of this method [10].

An alternative method is the so-called low-Reynolds-number modified k–ε model, which integrates the flow equations right up to the wall. With ready access to more powerful computer resources over the past decades, this method has attracted more attention for modelling turbulence of low-Reynolds-number flows. A number of such low-Reynolds-number k–ε models have been proposed [14–18]. While the standard k–ε model was found to over-predict the averaged wall heat transfer for tall vertical cavities [14], the predictions from the low-Reynolds-number k–ε models of Lam and Bremhorst [15], Chien [16], and Jones and Launder [17] were found to be reasonably close to the experimental measurements. Davidson [18] used a combination of low-Reynolds-number modifications partly from the models of Jones and Launder [17] and that of Lam and Bremhorst [15] in his 'hybrid' k–ε model to calculate the turbulent flow of air in the tall cavity of Cheesewright and co-workers [2–5]. Hanjalic et al. [1] recently studied a number of natural convection flows in empty and divided cavities with different aspect ratios, boundary conditions and partitions by employing the method of Jones and Launder [17]. This low-*Re*-number modification method of Jones and Launder is also adopted for the present study to account for the near wall effects.

1.2. Thermal turbulence

The importance of thermal turbulence, represented by the turbulent heat fluxes, has long been realised in the simulation of natural convection flows. Ince and Launder [8] employed the Generalised Gradient Diffusion Hypothesis (GGDH) to take into account the interaction of the Reynolds shear stresses and the span-wise temperature gradients. Hanjalic [9,11] suggested that the minimum level for modelling the turbulent heat flux in buoyancy driven flows should be the second-moment closure, including the interactions of the temperature variance and gravitational force, and of the heat flux itself and mean strain. Although the turbulence model of Hanjalic employed more complex second-moment closure, it only achieved marginal improvements in predicting the turbulent heat flux as compared with the two-equation k–ε model of Ince and Launder [8]. On the predictions of other turbulent quantities, it disagreed with the experimental data of Cheesewright and co-workers [2–5]. This may be attributed to the use of the eddy-viscosity (isotropic) assumption to depict the Reynolds stresses in the model. According to the experimental reports of Cheesewright et al. [2–5], the greatest gradient of temperature is in the horizontal direction, while the vertical heat flux is three times as much as the horizontal one. This implies that the anisotropy of turbulence has significant effects both on the turbulent heat flux and the Reynolds stresses in the buoyancy driven enclosure flows.

1.3. Reynolds stresses

Among the literature for turbulence modelling of buoyancy driven flows, little can be found on the non-isotropy of Reynolds stresses in either the two-equation type low-*Re*-number k–ε turbulence models or higher order turbulence models, e.g. the three-equation k–ε–$\overline{\theta^2}$ and four-equation k–ε–$\overline{\theta^2}$–ε_θ models of Hanjalic [1,9]. Although the Reynolds stress model in differential or algebraic form can account for the anisotropy of turbulence due to buoyancy and near wall effects, it has well known drawbacks: computationally expensive and numerically unstable [19,20]. When this model is used together with other complex equations of turbulent scalar quantities, the benefit of inclusion of the Reynolds stress model is overshadowed by the uncertainties involved in assigning values to the coefficients. Davidson [18] developed a 'hybrid' model for the Reynolds stresses by adding the buoyancy term of the algebraic Reynolds stress (ASM) model, as a second-order correction, to the eddy viscosity model (EVM) in a linear uncoupling manner. The ASM corrections were supposed to account for the non-isotropy of turbulence in buoyant flows. His results showed that the value of the second-order correction of Reynolds stresses is a few times as much as that of the eddy viscosity part in the near wall region. But the use of the Simple Gradient Diffusion Hypotheses (SGDH) for the turbulent heat flux had failed to improve the prediction significantly.

1.4. Pressure–strain correlation

The pressure–strain correlation is regarded as the most important process in turbulence modelling. The fluctuating pressure under the influences of buoyancy and presence of solid wall has significant effect on the behaviour of the Reynolds stresses and turbulent heat fluxes. Although the concept of 'return-to-isotropy' [21] and wall-reflection functions [22] was originally derived from intuition rather than strict mathematics, it still gives better results over a wide range of shear flows. Recently, Craft et al. [23] developed a new type of second-moment closure turbulence model with far

more complex expressions for the pressure–strain correlation. It is, however, hard to justify its stability and the physical meanings of the individual terms in the correlation.

1.5. Objectives of the paper

In the present study, a new buoyancy modified turbulence model has been developed. The model is based on the four-equation k–ε–$\overline{\theta^2}$–ε_θ turbulence model of Hanjalic [1]. The major contribution of the current study is the newly devised 'return-to-isotropy' concept. This is based on the common belief that high Reynolds number flows promote isotropy and low turbulence retains relatively strong anisotropy. The wall-reflection function for pressure-strain correlation is also modified to emphasise the buoyancy effects. Effects of anisotropy on the dissipative motion are considered by the method of Hanjalic [24].

For model validation, numerical computations have been performed for the experiments of Cheesewright and co-workers [2–5] in a tall air cavity of aspect ratio (height to width) 5 on the full set of the mean and turbulent quantities. A new set of experimental data for another elemental natural convection configuration, the square cavity [6,7], is also compared with the predictions from the present model. The present model has been found to be in reasonable agreement with both sets of experimental data. The predictions from the low-*Re*-number model of Ince and Launder [8], and Hanjalic's three- [9] and four- [1] equation models are also presented. The present model has demonstrated significant improvements in predicting the turbulent flow fields near the vertical walls in the buoyancy driven enclosure flows.

2. Mean flow equations

The Navier–Stokes differential equations for mass, momentum and energy can be written, in Cartesian coordinates, as

$$\frac{D\rho}{D_t} = 0 \tag{1}$$

$$\frac{D(\rho U_i)}{Dt} = D_i - \frac{\partial p}{\partial x_i} + \rho g_i \tag{2}$$

$$\frac{D(\rho T)}{Dt} = D_T \tag{3}$$

where

$$D_i = \frac{\partial}{\partial x_j}\left(\mu\frac{\partial U_i}{\partial x_j} - \rho\overline{u_i u_j}\right);$$

and

$$D_T = \frac{\partial}{\partial x_i}\left(\frac{\mu}{\sigma_t}\frac{\partial T}{\partial x_i} - \rho\overline{u_i\theta}\right).$$

The density is calculated by the ideal gas law.

3. Turbulence model

3.1. Governing equations

The following set of equations from Hanjalic [1] for turbulent quantities of k, ε, $\overline{\theta^2}$ and ε_θ constitutes the basic platform of the present model, as

$$\frac{D(\rho k)}{Dt} = D_k + \rho(P+G) - \rho\varepsilon \tag{4}$$

$$\frac{D(\rho\overline{\theta^2})}{Dt} = D_\theta + 2\rho P_\theta - 2\rho\varepsilon_\theta \tag{5}$$

$$\frac{D(\rho\tilde{\varepsilon})}{Dt} = D_\varepsilon + C_{\varepsilon 1}\rho(P+G)\frac{\tilde{\varepsilon}}{k} - C_{\varepsilon 2}f_\varepsilon\rho\frac{\tilde{\varepsilon}^2}{k} + E \tag{6}$$

$$\frac{D(\rho\tilde{\varepsilon}_\theta)}{Dt} = D_{\varepsilon_\theta} + C^\theta_{\varepsilon 1}\rho P\frac{\tilde{\varepsilon}_\theta}{k} + C^\theta_{\varepsilon 3}\rho P_\theta\frac{\tilde{\varepsilon}_\theta}{\overline{\theta^2}} - C^\theta_{\varepsilon 2}\rho\frac{\tilde{\varepsilon}_\theta^2}{\overline{\theta^2}} - C^\theta_{\varepsilon 4}f_{\varepsilon_\theta}\rho\frac{\tilde{\varepsilon}_\theta\tilde{\varepsilon}}{k} + E_\theta \tag{7}$$

where

$$P = -\overline{u_i u_j}\frac{\partial U_i}{\partial x_j}, \quad G = -\beta g_i\overline{u_i\theta}, \quad P_\theta = -\overline{u_j\theta}\frac{\partial T}{\partial x_j} \tag{8}$$

$$E = 2\mu\frac{\mu_t}{\rho}\left(\frac{\partial^2 U_i}{\partial x_j\partial x_k}\right)^2, \quad E_\theta = 2\rho\alpha\alpha_t\left(\frac{\partial^2 T}{\partial x_j\partial x_k}\right)^2 \tag{9}$$

$$\tilde{\varepsilon} = \varepsilon - 2\nu\left(\frac{\partial k^{1/2}}{\partial x_n}\right)^2, \quad \tilde{\varepsilon}_\theta = \varepsilon_\theta - \alpha\left(\frac{\partial(\theta^2)^{1/2}}{\partial x_n}\right)^2 \tag{10}$$

$$D_\phi = \frac{\partial}{\partial x_j}\left(C_\phi f_\mu\rho\frac{k^2}{\tilde{\varepsilon}}\frac{\partial\phi}{\partial x_j} + \mu\frac{\partial\phi}{\partial x_j}\right) \tag{11}$$

D_ϕ denotes the total diffusion term. The following coefficients [1] were adopted:

C_ε	$C_{\varepsilon 1}$	$C_{\varepsilon 2}$	$C^\theta_{\varepsilon 1}$	$C^\theta_{\varepsilon 2}$	$C^\theta_{\varepsilon_3}$	$C^\theta_{\varepsilon 4}$
0.07	1.44	1.92	0.72	2.2	1.3	0.8

The damping functions f_ε and $f_{\varepsilon\theta}$ in Eqs. (6) and (7) are as follows [1]: $f_\varepsilon = 1.0-0.3\exp(-Re_t^2)$ and $f_{\varepsilon\theta}=1$.

3.2. Turbulent heat flux

The algebraic expression [1] for the turbulent heat flux derived from its parent full transport equation is written, as

$$\overline{\theta u_i} = -C\frac{k}{\varepsilon}\left(\overline{u_i u_j}\frac{\partial T}{\partial x_j} + \xi\overline{\theta u_j}\frac{\partial U_i}{\partial x_j} + \eta\beta g_i\overline{\theta^2} + \varphi_{i\theta w}\right) \quad (12)$$

where $\varphi_{i\theta w}$ is the wall-reflection term [22] as follows:

$$\varphi_{i\theta w} = -c_{1\theta w}\frac{\varepsilon}{k}\overline{\theta u_k}n_k n_i\frac{k^{3/2}}{c_1\varepsilon x_n} \quad (13)$$

and x_n is the distance from the wall and n_i is the unit vector normal to the wall.

3.3. Reynolds stresses

The partial differential transport equation for Reynolds stresses is, as

$$\frac{D(\overline{u_i u_j})}{Dt} = D_{ij} + P_{ij} + G_{ij} + \varphi_{ij} - \varepsilon_{ij} \quad (14)$$

where the symbols of P_{ij} and G_{ij} denote the generation terms owing to shear and buoyancy, and D_{ij} is the total diffusion term.

The second-moment closure [24] of the dissipation rate tensor ε_{ij} is employed to account for the anisotropy of the turbulence dissipation motion, as

$$\varepsilon_{ij} = \varepsilon\left\{(1-f_s)\frac{2}{3}\delta_{ij} + \frac{\overline{u_i u_j}}{k}f_s\right\} \quad (15)$$

where $f_s=(1+0.1Re_t)^{-1}$

The pressure–strain term φ_{ij} can be traditionally decomposed into turbulence–turbulence interactions φ_{ij1}, mean strain contributions φ_{ij2} and buoyancy effects φ_{ij3}. The mathematical expressions for the pressure–strain correlation were originally introduced by using the linear 'return-to-isotropy' concept of Rotta [21]. This model has successfully described the isotropic trends of turbulence with the increases in Reynolds numbers. But for low-Reynolds-number flows, it overstates the isotropic effects of pressure fluctuations.

In the present study, instead of using complex mathematical descriptions for low-Reynolds-number flows, which are difficult to be justified for engineering applications, the low-Reynolds-number damping function f_μ of Jones and Launder [17] has been introduced to modify the coefficients in Rotta's model, as follows

$$\varphi_{ij1} = -c_1 f_\mu \varepsilon a_{ij} \quad (16a)$$

$$\varphi_{ij2} = -c_2 f_\mu\left(P_{ij} - \frac{2}{3}\delta_{ij}P\right) \quad (16b)$$

$$\varphi_{ij3} = -c_3 f_\mu\left(G_{ij} - \frac{2}{3}\delta_{ij}G\right) \quad (16c)$$

where

$$a_{ij} = \left(\overline{u_i u_j} - \frac{2}{3}\delta_{ij}k\right)/k;$$

and

$$f_\mu = \exp(-3.4/(1+Re_t/50)^2.$$

Following the previous investigator [26], two assumptions have been made in the development of the new model for Reynolds stresses:

- The total flux of the Reynolds stress ($C_{ij}-D_{ij}$), the sum of convection and diffusion fluxes in the transport equation for the Reynolds stress, is proportional to the total flux of the turbulent kinetic energy (C_k-D_k) [26], as

$$P_{ij} + G_{ij} + \varphi_{ij} - \varepsilon_{ij} = \frac{2}{3}\delta_{ij}(P+G-\varepsilon) \quad (17)$$

- The eddy viscosity model (EVM) represented by Eq. (18) can give appropriate estimation for the mean strain effects on Reynolds stresses, and the second-order correction (in the form of the algebraic Reynolds stresses model, ASM) due to buoyancy and near wall effects can be added to it.

$$(\overline{u_i u_j})_{EVM} = \frac{2}{3}\delta_{ij}k - \nu_t\left(\frac{\partial U_i}{\partial x_j} + \frac{\partial U_j}{\partial x_i}\right) \quad (18)$$

Accordingly, the new model for Reynolds stresses can be written in the following form:

$$\overline{u_i u_j} = (\overline{u_i u_j})_{EVM} + (\overline{u_i u_j})_{ASM} \quad (19)$$

The second order correction term $(\overline{u_i u_j})_{ASM}$, which accounts for the non-isotropy due to buoyancy and near wall effects, can be derived from Eqs. (15)–(17), as follows

$$(\overline{u_i u_j})_{ASM} = \frac{k}{\varepsilon}\frac{(1-c_3 f_\mu)}{(c_1 f_\mu + f_s)}\left(G_{ij} - \frac{2}{3}\delta_{ij}G\right) + \frac{k}{\varepsilon}\frac{1}{(c_1 f_\mu + f_s)}\varphi_{ijw} \quad (20)$$

The wall-reflection function φ_{ijw} is of the form of Gibson and Launder [22]:

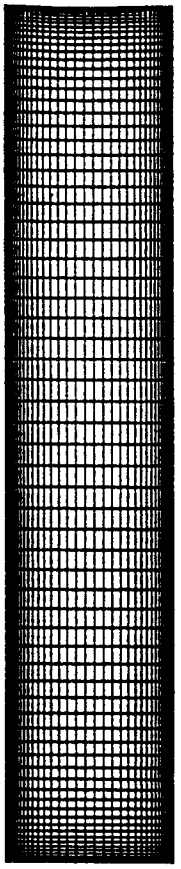

(a)

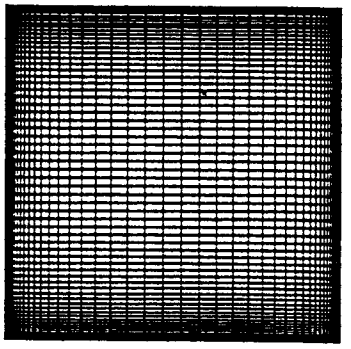

(b)

Fig. 1. Computational grids: (a) tall cavity; (b) square cavity.

Table 1
Specification of coefficients and constants

C	ξ	η	$c_{1\theta w}$	c_1	c_2	c_3
0.28	0.6	0.6	0.25	1.8	0.6	0.6
c_{1w}	c_{2w}	c_{3w}	c_l	c_μ	σ_t	
0.5	0.3	0.5	2.5	0.09	0.9	

$$\varphi_{ijw} = \frac{k^{3/2}}{c_1 \varepsilon x_n} \times \left\{ \begin{array}{l} c_{1w}\frac{\varepsilon}{k}\left(\delta_{ij}\overline{u_k u_m}n_k n_m - \frac{3}{2}\overline{u_k u_i}n_k n_j - \frac{3}{2}\overline{u_k u_j}n_k n_i\right) \\ +c_{2w}\left(\delta_{ij}\varphi_{km2}n_k n_m - \frac{3}{2}\varphi_{ik2}n_k n_j - \frac{3}{2}\varphi_{kj2}n_k n_i\right) \\ +c_{3w}\left(\delta_{ij}\varphi_{km3}n_k n_m - \frac{3}{2}\varphi_{ik3}n_k n_j - \frac{3}{2}\varphi_{kj3}n_k n_i\right) \end{array} \right\} \tag{21}$$

where the coefficient c_{3w} is given the value of c_{1w} to account for buoyancy effects. φ_{ij2} and φ_{ij3} in Eq. (21) are not modified by the damping function f_μ. It is common knowledge that the presence of the wall will increase the anisotropy of the Reynolds stress field by reducing the stress normal to it and enhancing the ones in the longitudinal directions. It is therefore appropriate to consider that the wall-reflection functions φ_{ijw} should behave differently to φ_{ij} of Eq. (16) and the original formula for φ_{ij} in Eq. (21) can produce the correct non-isotropic trends in the near wall region.

For the normal Reynolds stresses, the use of Eq. (21) in the second-order correction has balanced the need to emphasise the buoyancy and wall-reflection effects, redistributing the turbulence energy between the normal Reynolds stresses in the vicinity of the wall. However, the inclusion of the first group inside the brackets in Eq. (21) gave contrary predictions for the shear stress in the region near the vertical walls as compared with both sets of the cavity flow experimental data [5,7]. This is believed to be due to the fact that the shear stress $\overline{uv}$ is even greater than the normal stress $\overline{u^2}$ in the region near the vertical wall. To overcome this difficulty, the wall-reflection function for the shear stress φ_{ijw} $(i \neq j)$ is modified to include only the buoyancy effects, as

$$\varphi_{ijw} = -1.5 c_{3w} \frac{k^{3/2}}{c_1 \varepsilon x_n}(\varphi_{ik3}n_k n_i + \varphi_{kj3}n_k n_j) \quad \text{for} \quad i \neq j \tag{22}$$

Furthermore, it is considered that if the buoyancy is to increase the strength of turbulence when the vertical

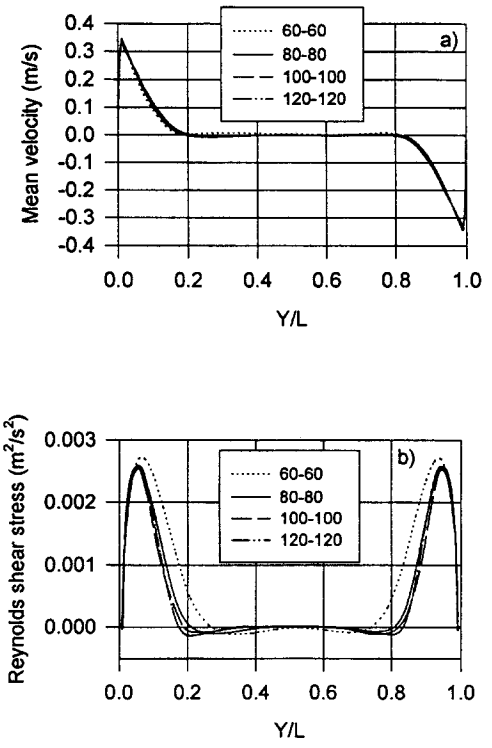

Fig. 2. Predicted profiles of the mean velocity and Reynolds shear stress at mid-height across the tall cavity with different grid sizes.

turbulent heat flux $\overline{\theta v}$ is greater than zero, the contributions from the vertical heat flux should bear the same weight on the modifications to the shear stress as the horizontal one. A new form of G_{i2} $(i \neq 2)$, the shear stress generation rate owing to buoyancy in the vertical plane, is proposed as:

$$G_{i2} = g\beta\overline{\theta u_i}\left(1 + \frac{\max[\overline{\theta v}, |\overline{\theta u_i}|]}{|\overline{\theta u_i}|}\right)/2.0 \tag{23}$$

It is worth pointing out that in the present model, the shear production (P) of the turbulent kinetic energy in the k equation (Eq. (4)), is still calculated by the eddy viscosity approach $(\overline{u_i u_j})_{\mathrm{EVM}}$ (Eq. (18)). Preliminary tests have shown that the inclusion of the second order correction in this term could cause enormous difficulty in convergence. Other researchers, e.g. Davidson [18], also reported similar experiences. This is thought to be caused by the strong coupling between mechanical turbulence and thermal turbulence in the second-moment closure. It should be noted that the proposed second-moment corrections for Reynolds stresses do not change the level of turbulence, i.e. the sum of the corrections for the normal Reynolds stress is zero. Instead, it only re-distributes turbulent energy between its components.

The constants in the Eqs. (12)–(20) are listed in Table 1 [1,22,25].

4. Numerical method

The SIMPLEC algorithm was adopted in the in-house research CFD code [27,28]. As is shown in Fig. 1, the 2-D computational grids are staggered and clustered toward the walls. Several grid sizes have been tested, i.e. 60 × 60, 80 × 80, 100 × 100 and 120 × 120. As can be seen in Fig. 2(a) and (b), little changes have been found in the predicted profiles of velocity and shear stresses at mid-height as the grid size increased beyond 80 × 80. Therefore, the grid size of 80 × 80 has been chosen for the final simulation reported here. The 'false-time-step' under-relaxation technique was used to achieve convergence, with typically a time step of 1 s. This was equivalent to 20 and 30 times the estimated residue time at each cell, $H/\sqrt{0.1g\beta\Delta TH}/NY$ (NY, number of cell in y-direction), for the tall and square cavities, respectively. Computations were assumed to have converged after the absolute residual mass source (over the whole computation domain) was less than 10^{-4} and the changes in any computing values at the monitoring point over a 10-iteration cycle were less than 0.5%. Approximately, between 10–50 sweeps per time step and totally 1500–2000 time steps were required to obtain the final steady-state solutions on a DEC Alpha 3000/400 workstation.

5. Experiments considered and boundary conditions

Two sets of experiments in air filled cavities have been considered. The first was a tall cavity of aspect ratio 5:1 with dimensions of 2.5 m (H) × 0.5 m (W) × 1.0 m (D), as used by Cheesewright et al. [2–5]. Two vertical walls with a distance of 0.5 m were maintained at nominally uniform temperatures of 77.5°C and 31.5°C. Special measures have been taken to insulate the top, bottom and other two side surfaces. It is widely acknowledged that it is very difficult to achieve real adiabatic conditions in an air filled cavity. The unidentified heat losses in these tall cavity experiments were estimated to be about 20% of total heat input into the cavity [2–5]. In a more recent computation reported by Ince and Launder [29], the heat losses through the non-isothermal walls were allowed and improved agreement with the experimental data was achieved. Such modifications to the boundary conditions have not been made in the present study as the main purpose of this paper is to illustrate the improvement obtained by the present model on the predic-

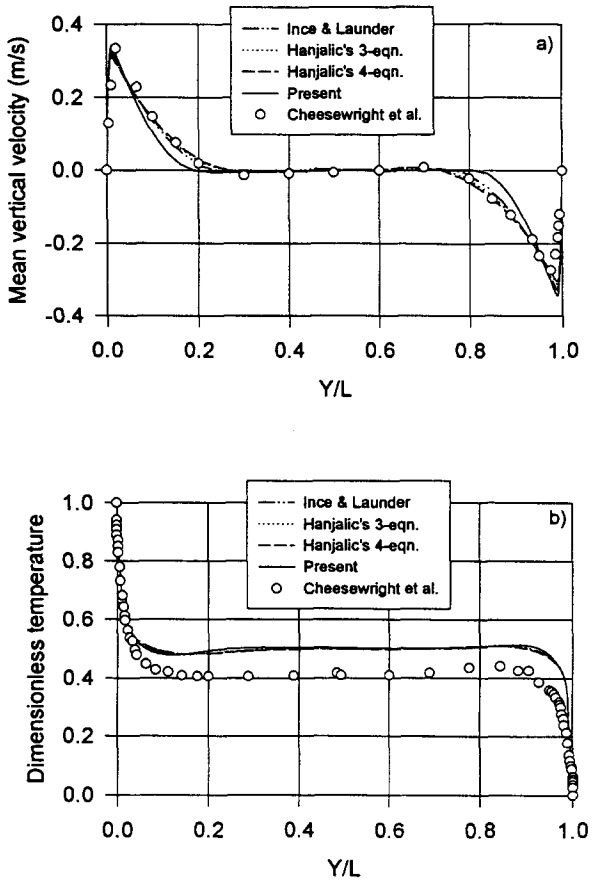

Fig. 3. Mean flow property distributions across the tall cavity at $x/H = 0.497$: (a) vertical velocity; (b) temperature.

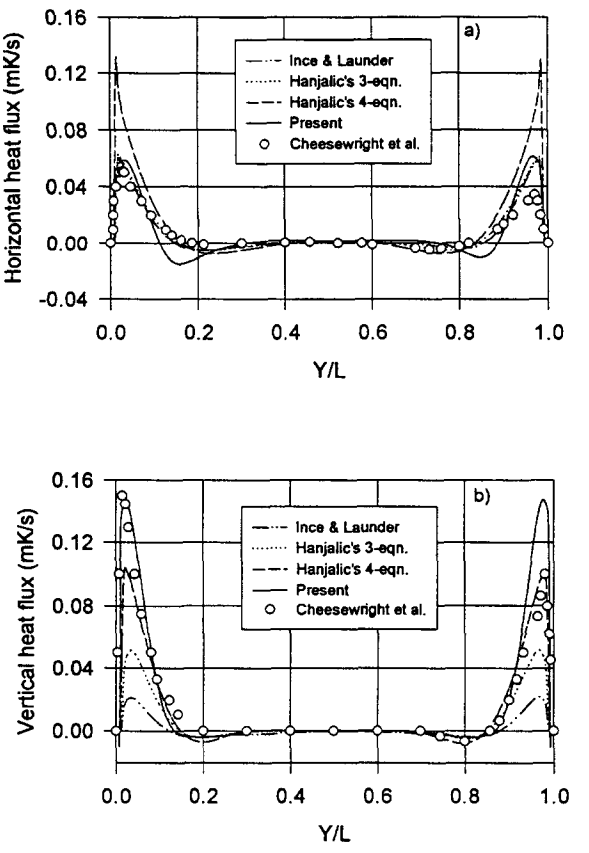

Fig. 4. Profiles of turbulent heat flux across the tall cavity at $x/H = 0.497$: (a) horizontal; (b) vertical.

tions of turbulent quantities in the vertical boundary layers.

The second case was a square cavity investigated by Tian and co-workers [6,7]. The cavity was 0.75 m (H) × 0.75 m (W) × 1.5 m (D) with two opposite isothermal walls at 50°C and 10°C giving a *Ra* number of 1.58×10^9. Unlike the case of Cheesewright, the horizontal walls, ceiling and bottom, were left to have sufficient heat transfer with the surrounding which was being maintained at a constant temperature of 30°C.

In both cases, the fixed temperature boundary conditions are imposed on the heating and cooling vertical walls: 77.5°C and 31.5°C for the tall cavity, and 50°C and 10°C for the square cavity, respectively. Adiabatic condition is specified on the horizontal walls of the tall cavity and the counterpart in the square cavity are treated as highly conductive walls.

6. Results and discussions

Numerical predictions were made for the two sets of experimental data using the present turbulence model as well as the low-Reynolds-number turbulence model of Ince and Launder [8] and Hanjalic's three- [9] and four- [1] equation turbulence models.

6.1. Case 1—tall cavity

In the first test case, i.e. the tall cavity of Cheesewright et al. [2–6], the comparisons were made for the mid-height considering that the imperfect boundary conditions on the top and bottom walls should not affect the mid-height distributions of parameters significantly. Fig. 3 shows the distributions of the mean properties. It is seen that the predictions from the four different turbulence models on the mean velocity and temperature profiles almost collapse on one curve across the cavity. The present model slightly under-predicted the vertical velocity boundary layer thickness. All the models have achieved reasonably

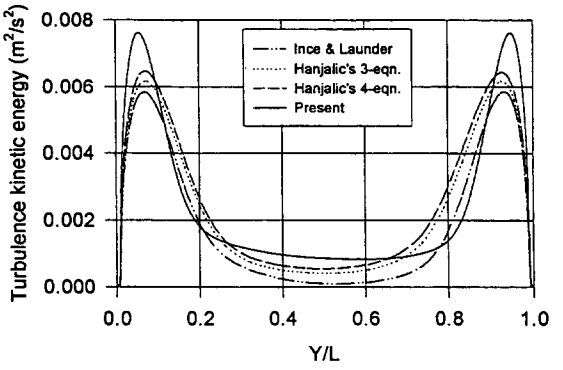

Fig. 5. Profiles of turbulent kinetic energy across the tall cavity at $x/H = 0.497$.

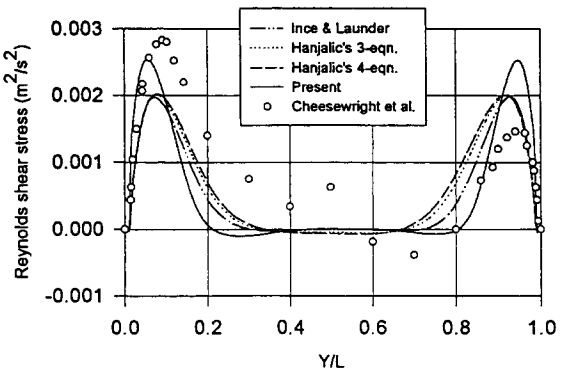

Fig. 6. Profiles of Reynolds shear stress across the tall cavity at $x/H = 0.497$.

good agreement with the experimental data. The predicted temperatures seem to be generally higher than the measured values. This discrepancy can be mainly attributed to the aforementioned heat losses through the top, bottom and side walls, which were estimated to be about 20% of the total heat input to the cavity [2–5]. Several other researchers, e.g. Ince and Launder [8], have also experienced the same problem. These heat losses had the effect of lowering the temperatures in the core region in the experimental data and it could also lead to an unequal drop of temperatures in the vertical boundary layers of the hot and cold walls. As a result, asymmetry of the turbulent quantity distributions was observed in the experimental data.

Fig. 4 is the comparison of predictions for the turbulent heat fluxes. The present model has achieved much closer agreement with the experimental data in the region near the hot wall. All the other three models over-predicted the horizontal turbulent heat flux, especially the Hanjalic's four-equation model, and under-predicted the vertical turbulent heat flux. Near the cold wall, the comparison has presented a rather complicated picture. All four models have predicted higher horizontal turbulent heat flux than the experimental data. For the vertical turbulent heat flux, the present model predicted higher values than the experimental data, and the Hanjalic three-equation model and the Ince and Launder model predicted lower values, while the Hanjalic four-equation model has the closest agreement with the experiments. Considering the asymmetry of the turbulence in the cavity due to the heat losses, the agreement obtained by the four-equation model of Hanjalic near the cold wall would be likely regarded as a coincidence rather than the model performance.

As shown in Fig. 5, all the models have predicted similar values for the total turbulent kinetic energy with predictions of the current model being slightly higher. As Cheesewright et al. [2–5] did not report on the measurement of this quantity, we can not make direct comparisons with the experimental data. For the shear stresses, as shown in Fig. 6, none of the models agree with the experiments. However, the peak value and distribution between the hot wall and the location of the peak value, as predicted by the present model,

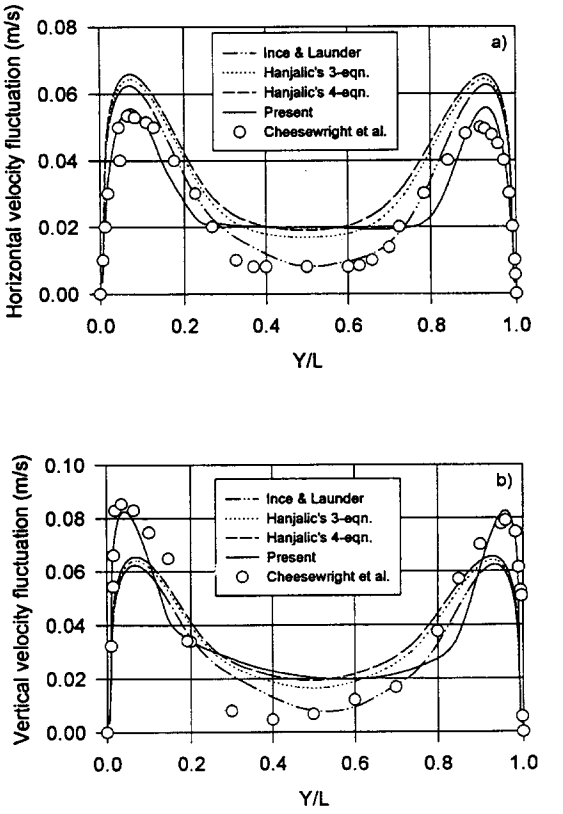

Fig. 7. Profiles of velocity fluctuations across the tall cavity at $x/H = 0.497$: (a) horizontal; (b) vertical.

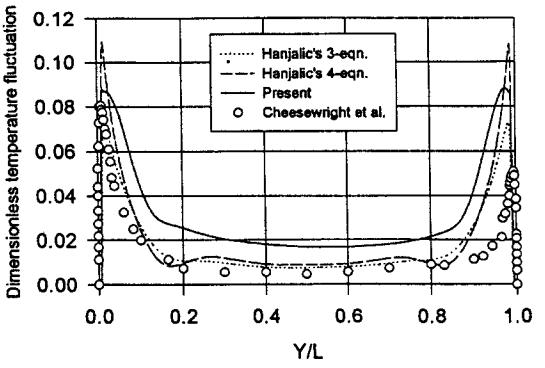

Fig. 8. Profiles of dimensionless temperature fluctuation across the tall cavity at $x/H = 0.497$.

are closer to the experimental data than the other three models. The poor agreement near the cold wall can again be attributed to the heat losses in the experiments.

A comparison of the predicted and measured horizontal and vertical velocity fluctuations is given in Fig. 7. It can be seen that the predictions of the present model are much closer to the experimental data in the vertical boundary layers. However, all the models, except for the Ince and Launder model, have over-predicted both the horizontal and vertical velocity fluctuations in the core region where the buoyancy and turbulence effects are not as strong as that in the vertical boundary layers. The damping functions adopted here for low-Reynolds-number turbulence were originally derived for the two-equation k–ε model. All the other three turbulence models, Hanjalic' three- and four-equation models and the present model, were

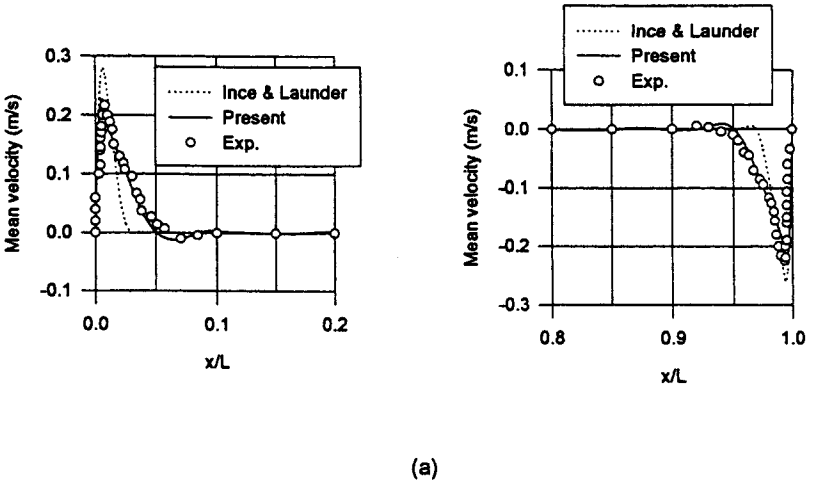

(a)

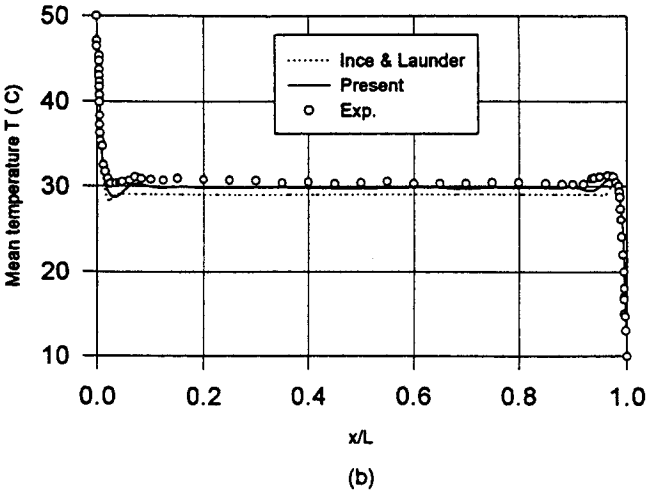

(b)

Fig. 9. Profiles of mean velocity and temperature at mid-height of the square cavity: (a) velocity; (b) temperature.

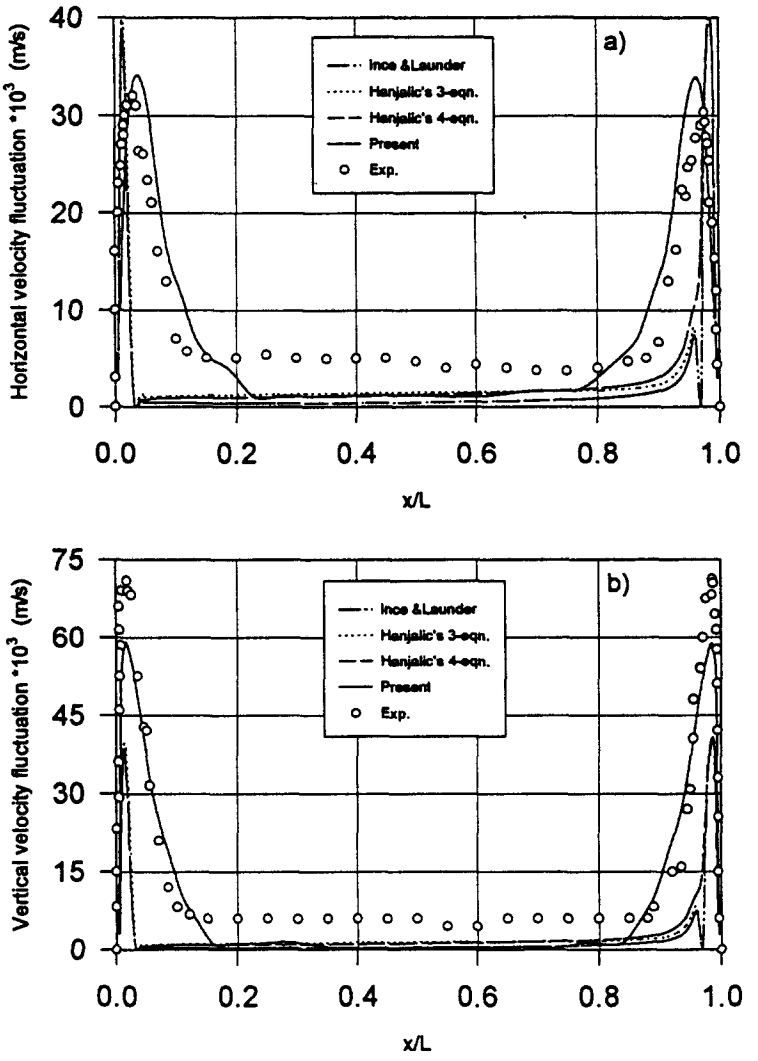

Fig. 10. Distributions of velocity fluctuations at mid-height of the square cavity: (a) horizontal; (b) vertical.

based on the solutions for the transport conservation equations for k, ε and $\overline{\theta^2}/\varepsilon_\theta$. This implies that the damping functions have not reduced the level of turbulence intensity enough for the free flow low-Reynolds-number effects in the core region.

In Fig. 8, the profiles of dimensionless temperature fluctuations across the cavity are plotted. It is seen that the present model, (Ince and Launder model is not included here, as it can not predict temperature variance), slightly over-predicted the temperature fluctuation at the hot wall boundary layer while Hanjalic' three-equation model slightly under-predicted the results. However, it is worth mentioning that predictions of the present model are still closer to the experiments than Hanjalic's four-equation model. This is encouraging as the present model is developed on the basis of that model. Due to the asymmetry of the experimental data caused by the unidentified heat losses through the non-isothermal surfaces, it is difficult to draw any specific conclusion from the comparison for the region near the cold wall. For this particular region, the comparison in the second test case, i.e. the square cavity with almost symmetrical boundary conditions, will be more reliable.

6.2. Case 2—square cavity

This is the square cavity tested by Tian *et al.* [6–7]. Fig. 9 presents the mean velocity and temperature predictions in comparison with the experimental data. Since the values of the mean velocities remain almost constant in the core region, only the velocity profiles in

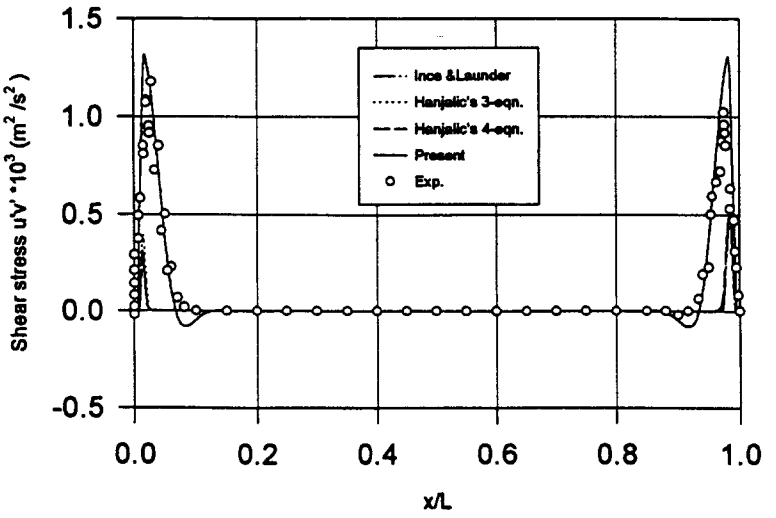

Fig. 11. Shear stress distributions at mid-height of the square cavity.

the regions near the hot and cold walls are plotted here. For the vertical velocity in Fig. 9(a), it is seen that the present model is in excellent agreement with the experimental data while the other three models give higher peak values. (As the predictions of the other three models are almost on top of each other, only the results from the model of Ince and Launder are plotted.) More importantly, the comparison has demonstrated that the present model has correctly predicted the vertical velocity boundary layer thickness. In Fig. 9(b), it can be seen that the temperature distributions predicted by the present model are also in reasonably good agreement with the experimental data. The other models have slightly under-predicted the mean temperature.

Similarly, as shown in Fig. 10, the present model has achieved significant improvement on the predictions of velocity fluctuations. All the other three models have over-predicted the horizontal fluctuation by 20% and under-predicted the vertical fluctuation by 40%.

In Figs. 11 and 12, the computations on shear stress and turbulent kinetic energy are plotted. The present model has also closely matched the experimental data while the shear stress predicted by the other three models are only about one third of the experimental

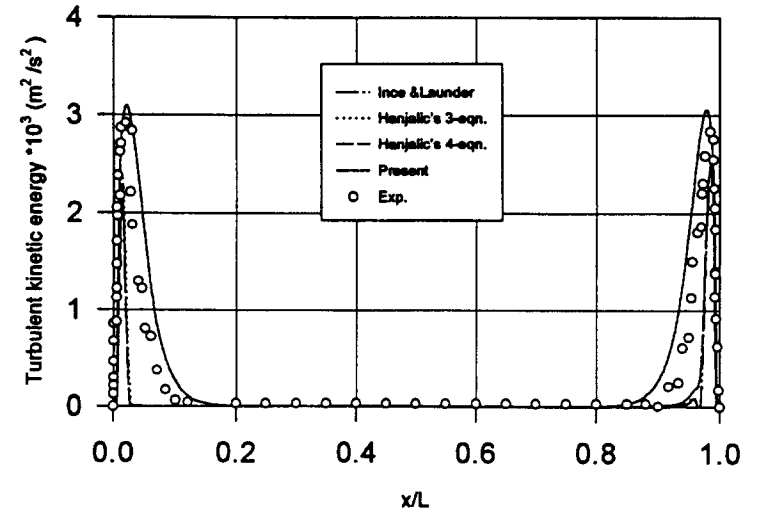

Fig. 12. Turbulent kinetic energy distribution at mid-height of the square cavity.

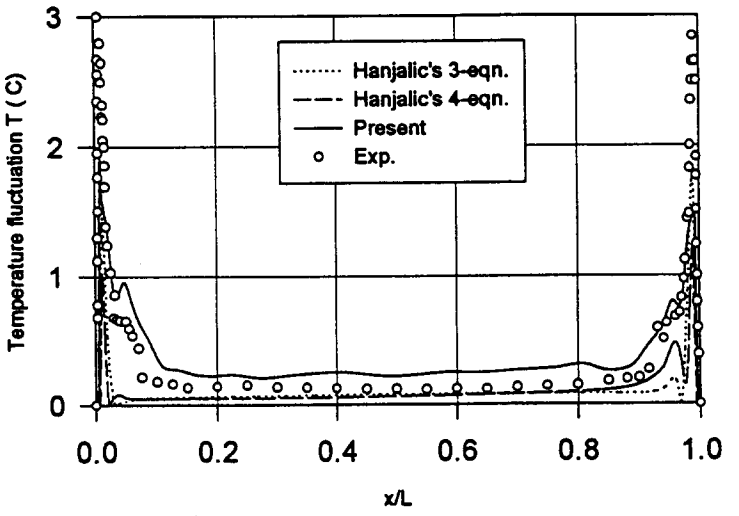

Fig. 13. Temperature fluctuations at mid-height of the square cavity.

value and the turbulent energy is under-predicted by about 20%.

As shown in Fig. 13, there are relatively large discrepancies between the predicted temperature fluctuations by all the models and that measured in the experiments. This is probably due to the improper description of the conservation transport process of the temperature variance dissipation rate, ε_θ. Further work is now under way to explore a more suitable form of ε_θ equation for buoyant flows.

Most importantly, the evidence from Figs. 10–13 has shown that the present model has correctly predicted the lateral extent of the turbulent boundary layer near the vertical walls. The predictions by the other three models have shown effectively zero flow in this region. In addition, the fluctuations of turbulent quantities predicted by the other three models fall rapidly to zero, as one goes away from the wall. The asymmetry of the turbulent quantities predicted by the three other models is appearing at the mid-height, more apparently in Figs. 10 and 13. This might be attributed to the fact that these models tended to produce such weak turbulence that the predicted turbulent fields became very sensitive to any changes in fluid properties.

Because of the almost symmetrical boundary conditions in the square cavity (unlike the Cheesewright's case which suffered asymmetry due to heat losses through the side, top and bottom surfaces), the present model predictions of the mean and turbulent quantities in the region near the cold wall of the square cavity are also in good agreement with the experimental data.

7. Conclusions

A new buoyancy-modified turbulence model has been developed. The new model has the same complexity level as Hanjalic's four-equation model [1], but it includes new modifications to account for buoyancy and wall-reflection effects in Reynolds stresses. It has also avoided the instability on the convergence of solution, which Reynolds stresses models often suffer.

The new model has been compared with three other turbulence models and the experimental data of Cheesewright et al. [2–5] in a tall cavity of aspect ratio 5 and of Tian et al. [6,7] in a square cavity. In both cases, the present model has obtained very encouraging agreement. The following major conclusions emerged from the current study.

1. The present model has demonstrated its capability to predict the lateral extent of the turbulent boundary layer near the vertical wall. Where as the turbulence models which adopt the eddy viscosity approach to describe the Reynolds stresses, have failed to predict this flow feature correctly (Figs. 9–13).
2. The present model has achieved significant improvement on the predictions of velocity fluctuations for the region near the vertical walls (Fig. 10).
3. None of the models considered have achieved agreement with the tall cavity data for Reynolds shear stresses. The predictions of the present model are, however, in excellent agreement with the square cavity data for both Reynolds shear stresses and turbulent kinetic energy (Figs. 6, 11 and 12). (The tall cavity data did not contain measurements for turbu-

lence kinetic energy.)

4. The present model has achieved much closer agreement with the experimental data for turbulent heat flux in the region near the hot wall. All the other three models over-predicted the horizontal turbulent heat flux and under-predicted the vertical turbulent heat flux (Fig. 4).
5. Except for the Ince and Launder model, all the other models (including the current one), have over-predicted both the horizontal and vertical velocity fluctuations in the core region for the tall cavity but under-predicted these quantities for the square cavity (Figs. 7 and 10).
6. The predictions from the current model for the turbulent quantities are symmetric. This is anticipated because of the almost symmetric boundary conditions. The turbulent quantities predicted by the other three models are, however, asymmetric (Figs. 10 and 12).

Further work is now under way to test the model on a wider range of test cases and to establish a more suitable form for the ε_θ equation.

References

[1] K. Hanjalic, S. Kenjeres, F. Durst, Natural convection in partitioned two-dimensional enclosures at higher Rayleigh numbers, Int. J. Heat Mass Transfer 39 (7) (1996) 1407–1427.

[2] R. Cheesewright, S. Ziai, Distributions of temperature and local heat-transfer rate in turbulent natural convection in a large rectangular cavity, in: Proceedings of the Eighth International Heat Transfer Conference, 1986, pp. 1465–1471.

[3] R. Cheesewright, K.J. King, S. Ziai, Experimental data for the validation of computer codes for the prediction of two-dimensional buoyant cavity flows, in: Proceedings of the ASME Meeting HTD, 1986, pp. 75–81.

[4] R. Cheesewright, A. Bowles, Direct measurements of the turbulent heat flux in a large rectangular air cavity, Experimental Heat Transfer 2 (1989) 59–69.

[5] R. Cheesewright, K.J. King, Stress distributions in turbulent natural convection in a rectangular air cavity, in: Proceedings of the Ninth International Heat Transfer Conference, 1990, pp. 161–167.

[6] Y.S. Tian. Low turbulent natural convection in an air filled square cavity, Ph.D thesis, South Bank University 1997.

[7] Y.S. Tian, T.G. Karayiannis, R.D. Matthews, J.X. Wen, Reynolds stresses in low turbulence natural convection in air filled square cavity, in: Proceedings of the Eleventh International Heat Transfer Conference, Korea, 1998.

[8] N.Z. Ince, B.E. Launder, On the computation of buoyancy-driven turbulent flows in rectangular enclosures, Int. J. Heat and Fluid Flow 10 (2) (1989) 110–117.

[9] K. Hanjalic, S. Vasic, Some further exploration of turbulence models for buoyancy driven flows, in: Proceedings of the Eighth International Symposium On Turbulent Shear Flows, Germany, 1991, pp. 319–341.

[10] R.A.W.M. Henkes, C.J. Hoogendoorn, Numerical determination of wall functions for the turbulence natural convection boundary layer, Int. J. Heat Mass Transfer 33 (1990) 1087–1097.

[11] K. Hanjalic. Achievements and limitations in modelling and computation of buoyant turbulent flows and heat transfer. In: Proceedings of the Tenth International Heat Transfer Conference, 1995. 1. p. 1–18.

[12] W.K. George, S.P. Capp, A theory for natural convection turbulent boundary layers next to heated surfaces, Int. J. Heat Mass Transfer 22 (1979) 813–826.

[13] R. Cheesewright, The scaling of turbulent natural convection boundary layers in the asymptotic limit of infinite Grashof number, Euromech. Colloquium 207 (1986) (The Netherlands).

[14] R.A.W.M. Henkes, C.J. Hoogendoorn, Comparison of turbulence models for the natural convection boundary layer along a heated vertical plate, Int. J. Heat Mass Transfer 32 (1989) 157–169.

[15] C.K.G. Lam, K.A. Bremhorst, A modified form of the k–ε model for predicting wall turbulence, J. Fluid Engng 103 (1981) 456–460.

[16] K.Y. Chien. Predictions of channel and boundary layer flows with a low-*Re*-number two-equation model of turbulence, AIAA-80-0134 (1980).

[17] W.P. Jones, B.E. Launder, The prediction of laminarization with a two-equation model of turbulence, Int. J. Heat Mass Transfer 15 (1972) 301–314.

[18] L. Davidson, Second-order corrections of the k–ε model to account for non-isotropic effects due to buoyancy, Int. J. Heat Mass Transfer 33 (1990) 2599–2608.

[19] P.G. Huang, M.A. Leschziner, Stabilisation of recirculating-flow computations performed with second-moment closures and third-order discretization, in: Proceedings of the Fifth International Symposium On Turbulent Shear Flows, 1985, pp. 20.7–20.12 (Cornell).

[20] M.A. Leschziner. Numerical implementation and performance of Reynolds-stress closures in finite-volume computations of recirculating and strongly swirling flows, Lecture notes to Introduction to the Modelling of Turbulence, von Karman Institute for Fluid Dynamics 1987.

[21] J.C. Rotta, Statistiche theorie nichthomogener turbulenz: 1, Z. Phys. 129 (1951) 547–572.

[22] M.M. Gibson, B.E. Launder, Ground effects on pressure fluctuations in the atmospheric boundary layer, J. Fluid Mech. 86 (1978) 491–511.

[23] T.J. Craft, N.Z. Ince, B.E. Launder, Recent developments in second-moment closure for buoyancy-affected flows, Dynamics of Atmospheres and Oceans 23 (1996) 99–114.

[24] K. Hanjalic, S. Jakirlic, A model of stress dissipation in

second-moment closures, Applied Scientific Research 51 (1993) 513–518.

[25] K. Hanjalic, S. Vasic, Computation of turbulent natural convection in rectangular enclosures with an algebraic flux model, Int. J. Heat Mass Transfer 36 (1993) 3603–3624.

[26] B.E. Launder, in: P. Bradshaw (Ed.), Topics in Applied Physics, Springer, Berlin, 1976, p. 12.

[27] J.X. Wen, F. Liu, T.G. Karayiannis, R.D. Matthews, Numerical modelling of buoyancy-driven natural convection induced by fire in a compartment, in: Proceedings of the Heat Transfer Science and Technology Conference, Beijing, 1996, pp. 576–579.

[28] F. Liu, J.X. Wen, T.G. Karayiannis, R.D. Matthews, Computations of turbulent natural-convection flows in cavity with buoyancy-modified turbulence models, in: Proceedings of the Fifth UK National Conference on Heat Transfer, London, 1997.

[29] Z. Ince, B.E. Launder, Three-dimensional and heat loss effects on turbulent flow in a nominally two-dimensional cavity, Int. J. Heat and Fluid Flow 16 (1995) 171–177.